JGR Space Physics

RESEARCH ARTICLE
10.1029/2024JA032924

Special Collection:
Recent Discoveries in Substorm Research

Obtaining Continental-Scale, High-Resolution 2-D Ionospheric Flows and Application to Meso-Scale Flow Science

Y. Nishimura[1], L. R. Lyons[2], Y. Deng[3], C. Sheng[3], W. A. Bristow[4], E. F. Donovan[5], V. Angelopoulos[6], and N. Nishitani[7]

[1]Department of Electrical and Computer Engineering and Center for Space Physics, Boston University, Boston, MA, USA, [2]Department of Atmospheric and Oceanic Sciences, University of California, Los Angeles, Los Angeles, CA, USA, [3]Department of Physics, University of Texas, Arlington, TX, USA, [4]Pennsylvania State University, University Park, PA, USA, [5]Department of Physics and Astronomy, University of Calgary, Calgary, AB, Canada, [6]Department of Earth, Planetary, and Space Sciences, University of California, Los Angeles, Los Angeles, CA, USA, [7]Institute for Space Earth Environmental Research, Nagoya University, Nagoya, Japan

Key Points:

- High-resolution convection maps in the nightside high-latitude ionosphere were created with small errors and good agreement with Defense Meteorological Satellite Program
- The convection maps revealed a dynamic interplay of multiple flow channels during a substorm, including precursor flows to substorm onset
- The meso-scale flows contribute to ~10%–40% of the total flows on average. The contribution increases up to 73% during flow bursts

Correspondence to:
Y. Nishimura,
toshi16@bu.edu

Citation:
Nishimura, Y., Lyons, L. R., Deng, Y., Sheng, C., Bristow, W. A., Donovan, E. F., et al. (2024). Obtaining continental-scale, high-resolution 2-D ionospheric flows and application to meso-scale flow science. *Journal of Geophysical Research: Space Physics*, *129*, e2024JA032924. https://doi.org/10.1029/2024JA032924

Received 29 MAY 2024
Accepted 11 AUG 2024

Abstract An approach for creating continental-scale, multi-scale plasma convection maps in the nightside high-latitude ionosphere using the spherical elementary current systems technique has been developed and evaluated. The capability to reconstruct meso-scale flow channels improved dramatically, and the velocity errors were reduced by ~30% compared to the spherical harmonic fitting method. Uncertainties of velocity vectors estimated by varying the model setup was also low. Convection maps for a substorm event revealed multiple flow channels in the polar cap, dominating the convection in the quiet time and early growth phase. The meso-scale flows extended toward the nightside auroral oval and had continuous flow channels over >20° of latitude, and the flow channels dynamically merged and bifurcated. The substorm onset occurred along one of the flow channels, and the azimuthal extent of the enhanced flows coincided with the initial width of the auroral breakup. During the expansion phase, the meso-scale flows repetitively crossed the oval poleward boundary, and some of them contributed to subauroral polarization streams enhancements. Increased flows extended duskward, along with the westward traveling surge. Then, flows near midnight weakened and evolved to the Harang flow shear. The meso-scale flow channels had significant (~10%–40% on average) contributions to the total plasma transport. The meso-scale flows were highly variable on ~10 min time scales and their individual maximum contributions reached upto 73%. These results demonstrate the capability of specifying realistic convection patterns, quantifying the contribution of meso-scale transport, and evaluating the relationship between meso-scale flows and localized auroral forms.

1. Introduction

Plasma convection is one of the most fundamental processes in the geospace system. In the presence of magnetic field perturbations, it signifies electromagnetic energy transfer in terms of Poynting flux. In the ionosphere and thermosphere, convection redistributes plasma density, promotes Joule heating, and facilitates momentum exchange between plasma and neutrals via ion drag (see reviews by Nishimura, 2021; Nishimura et al., 2021). The large-scale two-cell convection pattern represents the dominant mode of global transport under a southward interplanetary magnetic field (IMF), but convection also involves meso-scale flow channels that have narrower (~100s of km) widths, exhibiting multi-scale convection structures. In the nightside high-latitude ionosphere, polar cap flow channels are embedded in large-scale anti-sunward convection in association with polar cap patches and arcs (Lyons et al., 2016). Polar cap flow channels reach the poleward boundary of the nightside auroral oval and trigger poleward boundary intensifications (PBIs), the ionospheric counterpart of magnetotail reconnection (de la Beaujardiere et al., 1994). The poleward boundary of the substorm auroral bulge is the region of active discrete aurora, where a strong flow shear is expected to occur. Auroral streamers are approximately north-south aligned arcs that emanate from PBIs and the poleward boundary of the bulge, and generally move equatorward. A streamer marks an upward field-aligned current sheet, and typically has a fast equatorward flow channel just dawnward of it (Gallardo-Lacourt et al., 2014). A flow channel is an ionospheric manifestation of a plasma sheet flow burst (e.g., Ferdousi et al., 2021). Flow channels associated with streamers (i.e., those that start at the poleward boundary) can occasionally reach the equatorward boundary of the auroral oval. When they do, they can intensify subauroral polarization streams (SAPS) (Gallardo-Lacourt et al., 2014).

Modeling of high-latitude convection has a long history. In situ observations along satellite tracks have resulted in statistical models of convection (Heppner & Maynard, 1987; Weimer, 2005). The spherical harmonic fit (SHF) technique fits line-of-sight (LOS) Doppler velocity measurements by ground-based radars such as the Super Dual Auroral Radar Network (SuperDARN) (Ruohoniemi & Baker, 1998; Thomas & Shepherd, 2018) by merging a statistical convection model and LOS observations to reconstruct time-dependent convection patterns. SHF has been used extensively, including the investigation of convection during substorms (Grocott et al., 2009, 2010).

However, statistical convection models are parameterized by the IMF. As a result, they have difficulty with expressing dynamical variations of convection that do not correlate well with the IMF. Moreover, SHF typically uses the 8th-order spherical harmonic functions, meaning that structures with a size smaller than a 3-hr MLT size are smeared out. Similarly, the Assimilative Mapping of Ionospheric Electrodynamics (AMIE) technique uses the 10-th-order spherical harmonic functions for creating convection patterns from velocity, magnetic field and precipitation measurements (Richmond & Kamide, 1988), making it difficult to resolve convection structures less than ∼2.4 hr MLT in size.

Attempts have been made to build convection maps that express both large and meso-scale flows. Merging flow measurements and statistical convection models improves performance in describing localized flows within the large-scale convection pattern (Ozturk et al., 2020; Wu & Lu, 2022). The Global, Local Divergence Free Fitting (G-LDFF) technique (Bristow et al., 2022) combines the high-resolution divergence-free flows and statistical convection models, and resolves localized flow structures in SuperDARN data more realistically. However, since those methods rely on statistical convection models, the convection patterns are still affected by the limited accuracy of the statistical convection model. Incoherent scatter radars can resolve localized flow structures without reliance on global convection models (Nicolls et al., 2014), but their fields-of-view (FOVs) are much smaller than SuperDARN's FOVs, so that only a small region, much less than a continental scale, can be measured simultaneously. LOS velocities alone have successfully resolved flow channels (Gabrielse et al., 2018; Nishimura, Lyons, Zou, Xing, et al., 2010; Nishimura et al., 2014), but it is difficult to discern flow orientation or connections between flows in adjacent echo regions. The Lompe technique can provide realistic convection without the need for background convection models by combining various data sets (Laundal et al., 2022), but meso-scale flow structures could be underestimated since typically not all data sets have high spatial and temporal resolution. Inaccurate specification of convection breaks consistency between convection and precipitation structures, resulting in large errors in the specification of ionospheric and thermospheric states (Sheng et al., 2019).

The present study aims to examine the evolution of meso-scale flow channels on a continental scale and quantify their contributions to the total flows in the nightside high-latitude ionosphere. We have extended the spherical elementary current systems (SECS) method (Amm et al., 2010; Vanhamäki & Juusola, 2020) to reconstruct high-resolution convection on a continental scale without any dependence on statistical convection models or the degree of spherical harmonic functions. We applied the method to a substorm event on 26 March 2014, where the THEMIS ASIs and SuperDARN radars covered much of the substorm activity. Previous investigations of this substorm event have already demonstrated the presence and utility of the favorable auroral and radar data coverage for identifying localized auroral and flow channels (Bristow et al., 2022; Lyons et al., 2019, 2022). Sections 3.1 and 3.2 quantify uncertainties of the SECS convection maps. Sections 3.3–3.5 show the evolution of the flow structures and the contributions of meso-scale flow channels to the total convection on continental scales in the nightside high-latitude ionosphere. SHF and SECS flows are also compared to evaluate improvements and limitations for specifying convection.

2. Data and Methods

2.1. Data

The THEMIS ASIs measure white-light auroral intensity every 3 s with a spatial resolution near the zenith of ∼1 km (Mende et al., 2008). The ASI data are mapped nominally onto a 110 km altitude plane, a typical emission height for ∼10 keV electron precipitation. Figure 1 shows a representative snapshot of the ASI mosaic in grayscale during the substorm growth phase on 26 March 2014. The auroral structures connected almost smoothly across the boundaries between the ASI FOVs, validating the choice of the mapping altitude.

The SuperDARN radars measure LOS velocities of ionospheric plasma every 1–2 min with a 45 km range resolution (Chisham et al., 2007). Figure 1a shows the LOS echo distribution in North America as colored vectors.

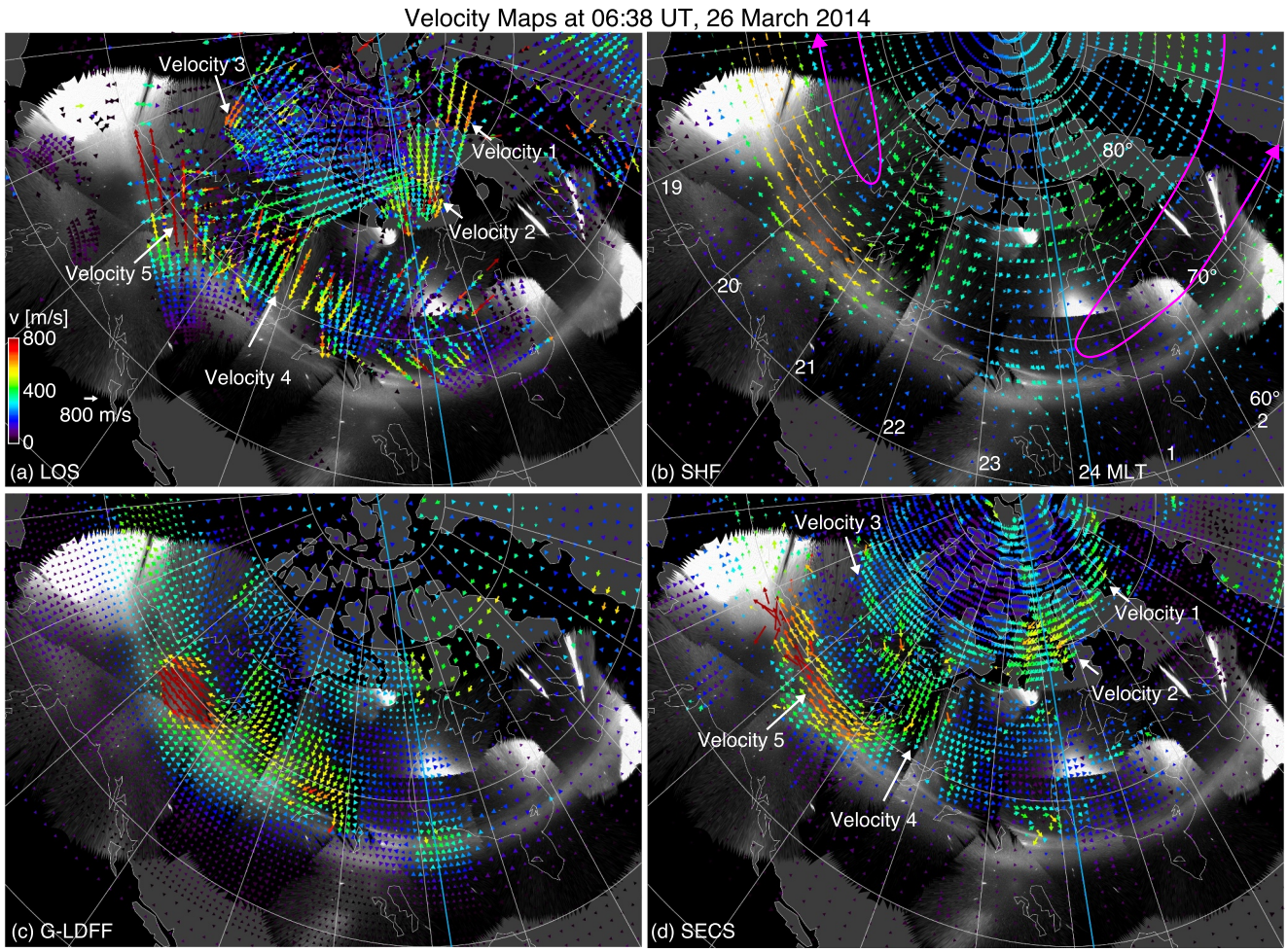

Figure 1. Maps of SuperDARN data (colored vectors) overlaid onto the THEMIS ASI data (grayscale, white being the brightest) at 06:38 UT on 26 March 2014. The panels shown are the velocity maps of (a) LOS, (b) spherical harmonic fit, (c) Global, Local Divergence Free Fitting, and (d) spherical elementary current systems. The thick and thin vectors in panels (b–d) indicate grid points with and without LOS echoes. The magenta lines in panel (b) illustrate the two-cell convection.

While SuperDARN radar echoes in the nightside auroral oval are often sparse, the radar echoes during this event had remarkable coverage over much of the nightside high-latitude ionosphere. The LOS velocities show localized enhancements indicated by the white arrows. The THEMIS ASIs provided auroral observations over nearly 8 hr of continuous local time coverage. This wide ASI and radar coverage allows for the identification of how the plasma flows are related to the location of the auroral oval and localized auroral structures.

The Defense Meteorological Satellite Program (DMSP) satellites measure cross-track plasma velocity along their polar orbits. The DMSP satellites generally orbit on the dayside when North America is on the nightside, but their magnetic footprints mapped from the southern hemisphere paths traverse North America. The satellite cross-track direction often had a large angle from the 2-D flow vectors in the convection map, but we identified a path whose cross-track direction was close to the 2-D flow vectors. That satellite path was used for validating the accuracy of the SECS flows.

2.2. Regional Divergence-Free Flow Reconstruction

The SECS method (Amm et al., 2010) was originally developed for divergence-free ionospheric horizontal currents from ground magnetometers (Amm & Viljanen, 1999), and was later applied to ionospheric flows. The basic principle of the SECS method is that the ionospheric flows are divergence-free ($\nabla \cdot \boldsymbol{v} = 0$), considering that ionospheric plasma is incompressible for the scale of interest (Bristow et al., 2022; Cowley, 2000; Southwood & Kivelson, 1993).

The SECS method does not directly solve $\nabla \cdot \boldsymbol{v} = 0$ because it is computationally expensive and requires a boundary condition. Instead, a divergence-free flow field is constructed by solving a matrix equation,

$$TI = Z \tag{1}$$

where Z is a 1-D array, and Z_i is the ith LOS velocity that is recorded within a 2-min time window. Poles (centers) of elementary divergence-free flow vortices are placed in the regions with radar echoes. The separation between poles in regions with dense echoes is 0.5° × 1.5° in latitude and longitude (~60 × 60 km at 70° latitude), comparable to radar range resolution, while fewer poles are placed in regions with sparse echoes. The pole separation determines the smallest scale size of flows to reconstruct. The pole distribution is determined by the echo distribution at each time, and this adaptive pole placement allows us to take advantage of dense echo coverage at each time. I is a 1-D array where I_j is the strength of the jth pole. I_j creates a divergence-free vortical flow around the pole $v_j = I_j/4\pi\alpha r$, where r is the distance from the pole, and α is a geometric factor. T is a geometrical transformation matrix where T_{ij} describes the direction of divergence-free flow velocity that is created by the jth pole along the LOS of the ith data point.

Equation 1 is solved for I using the singular value decomposition (SVD) as an optimization method (Strang, 2016). Although the equation may have more than one solution or no exact solution, SVD finds a solution that expresses large-scale flows more accurately and suppresses small-scale and weak flows that could be noise. Singular values less than 4% of the largest singular values were eliminated to remove such small-scale and weak flows. We varied this threshold between 1% and 6% and confirmed that the reconstructed convection maps were not affected largely by the choice of the threshold. A larger threshold resulted in a smoothed convection pattern that had large differences from the LOS velocity pattern, while a smaller threshold did not change the overall convection pattern but introduced unrealistic small-scale flow structures due to noise and edge effects of LOS echo coverage. SVD has also been applied to other space physics subjects such as GPS data processing (Fan & Ma, 2014). For the solution to converge, the array size of I should be smaller than the size of Z, and the radar echoes should cover a good portion of the region of interest. Once I is determined, 2-D velocity vectors can be determined at any desired locations as a sum of the vortical flows from all poles. We used a 0.5° × 0.1 hr MLT spherical grid system for visualization of the SECS 2-D flow vectors (this grid system does not affect the solution of Equation 1). This procedure is repeated for each UT.

LOS data at the first 8 range gates were excluded to eliminate E-region echoes. Isolated echoes (regions with only a few echoes) are removed to avoid spurious flow structures. The SECS method does not require echoes in a common volume. Although the velocity perpendicular to each LOS is not measured, the LOS velocity pattern over >16 beams carries information on 2-D flow vectors that are projected along each LOS (Makarevich & Dyson, 2007). Thus a minimum of one radar observation can be used to reconstruct flows within available data coverage.

Earlier works showed the capability of SECS for reconstructing convection in small regions covered by SuperDARN radars with a common volume (Amm et al., 2010) and large-scale electrodynamics in combination with various observations (Laundal et al., 2022). We extended the method to reconstruct flows over a continental scale using a maximum of 17 radars covering North America. We set the high spatial resolution to express both continental-scale and meso-scale convection together, but only used SuperDARN to avoid smearing out localized 2-D structures that SuperDARN can resolve better than other large-scale observables (such as currents and conductances). In Amm et al.'s work, their pole locations were not constrained by radar echoes, and poles far from LOS data contributed to large uncertainties. Our method placed poles only in the region of radar echoes at each time to improve the accuracy of flow reconstruction.

The SECS method has several advantages compared to other approaches. (a) SECS does not use any background convection models. SECS does not assume how background convection should vary with solar wind parameters. Thus SECS is free from uncertainties in statistical convection models and can describe dynamic variability of flows that does not correlate with solar wind parameters. (b) SECS does not use spherical harmonic functions. SHF and AMIE use the spherical harmonic functions, where the smallest flow structures are limited by the order of the spherical harmonic functions (the 8th order gives >3 hr local time size). SECS can reconstruct meso-scale convection features as small as the pole separation (0.5° × 1.5° size). (c) SECS does not use any boundary conditions. Models that solve electrostatic potential require a zero-potential boundary at the outer boundary

(Heppner-Maynard boundary for SHF). The location of the outer boundary affects how much a flow pattern expands to lower latitudes. SECS does not require a boundary but allows flows to close at any latitude.

Figures 1b and 1d compare SHF (Thomas & Shepherd, 2018) and SECS convection maps at 06:38 UT on 26 March 2014. The SHF convection map is dominated by a large-scale two-cell convection pattern. The LOS velocity map in Figure 1a shows enhanced and localized LOS velocities above 75° MLAT (Velocity 1, 2 and 3). The poleward boundary of the auroral oval was found at ∼68° MLAT, and thus those enhanced velocities were located in the polar cap. The SHF velocities in the polar cap were dominated by large-scale flows, and the localized nature of the LOS flows was essentially smeared out. In contrast, the SECS convection map reconstructed equatorward flow channels of ∼1 hr MLT width. Namely, SECS successfully reproduced multiple polar cap flow channels that the LOS velocity map suggests. The flow speed for Velocity 2 is comparable to the LOS speed. SECS somewhat underestimated the speed for enhanced Velocity 1 and 3, likely because they were surrounded by slower flows. Velocity 1 and 3 were located near the edges of the echo coverage, and thus the actual flow width could be wider. Nevertheless, SECS adequately represents the flow gradients within the echo coverage.

The multiple flow channels in the polar cap reconfigured to two flow channels at ∼74° MLAT at 21 and 23.5 hr MLT in the SECS convection map (Velocity 4). The flow channel at 21 hr MLT further extended equatorward and then turned duskward in the auroral oval, consistent with the Harang flow shear, typical at this MLT sector. SHF only shows a broad anti-sunward flow of a ∼3 hr MLT width at this latitude. Both SECS and SHF reproduced the enhanced duskward flow at ∼70° MLAT (Velocity 5), but SHF provided a weaker and broader flow channel.

Figure 1c presents the G-LDFF velocity map for reference. High-resolution grids for this version were placed between dusk and midnight. Overall, both SECS and G-LDFF can reproduce localized flow structures for most regions where they are expected based on the LOS velocity. Velocity 2 and 3 are represented as localized flow channels in a similar manner to SECS. The flow enhancements for Velocity 4 and 5 are also seen, although the flow channels are somewhat wider than the LOS velocity suggests. Velocity 1 was located outside the high-resolution grids and appears as a weak enhancement in the low-resolution grid. SECS uses the adaptive grid system based on the echo distribution at each time, and therefore resolved this flow channel within the high-resolution grids. The removal of background convection models in SECS could also contribute to the ability to show flow structures more clearly. More details of the G-LDFF velocity maps and validation for this event can be found in Bristow et al. (2022).

This example demonstrates that the SECS convection map reveals the spatial structure of convection that is expected from the LOS velocity map. More comparisons between SHF and SECS are presented in Sections 3.2 and 3.3. Despite the advantages of SECS, it is not appropriate for global convection patterns, because a statistical convection model is not used, and flow solutions away from radar echoes are not reliable. SECS focuses on regional convection when and where dense echo coverage exists. The flow solution is noisier when echoes are sparse, and SECS outputs are not constrained well outside echo coverage (thin vectors in Figure 1d). For example, there are few echoes around 76° MLAT near midnight in Figure 1a. This gap introduces uncertainties about how the flow channels above 78° MLAT and below 76° MLAT are connected to each other. SECS outputs in regions of echo coverage gaps are unreliable and should not generally be used to derive conclusions.

In addition, SuperDARN itself has limitations for estimating ionospheric flow velocity. SuperDARN tends to underestimate plasma flow velocity because the index of refraction is not routinely corrected (Gillies et al., 2018; Koustov et al., 2016), and radar echo locations have uncertainties due to the unknown density distribution along the signal raypath (Yeoman et al., 2008). Furthermore, some echoes are largely contaminated by various noise sources. Corrections of such known issues about SuperDARN are beyond the scope of the present study, as we aim to reconstruct high-resolution convection patterns within the current capability of SuperDARN. In Sections 3.1 and 3.2, we estimate uncertainties of the output velocity using various model setups, and we compare the output velocity to DMSP observations.

3. Results

3.1. Uncertainty Analysis

We created SECS convection maps every 2 min during 5–10 UT on 26 March 2014, a period with dense radar echo coverage. The flow evolution is discussed in Sections 3.3–3.5. Before presenting the scientific analysis of

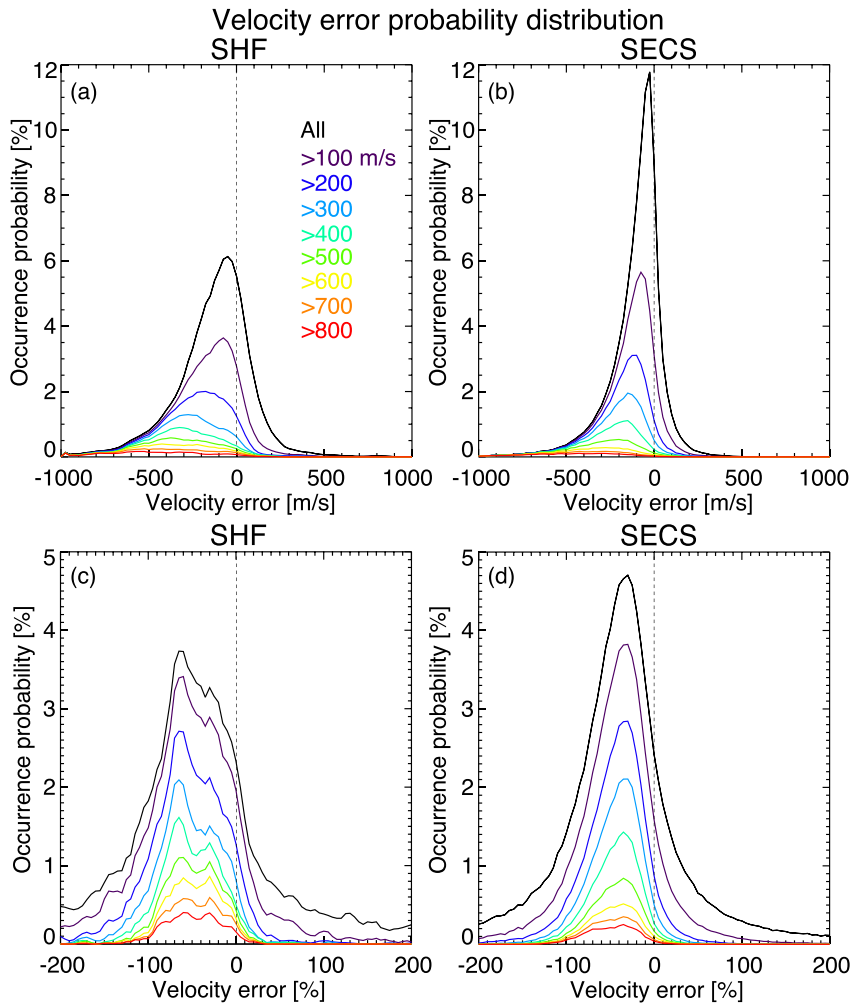

Figure 2. Occurrence probability distributions of the velocity errors in (a, b) m/s and (c, d) percentage. Panels a and c are for spherical harmonic fit, and panels b and d are for spherical elementary current systems.

the data, here we provide error estimates of the SECS flows. Figure 2b evaluates the performance of SECS flows by calculating the difference between the SECS velocity projected to the LOS direction and the measured LOS velocity. The velocity difference was obtained at each LOS echo location at each time, and all data points were combined to create the occurrence probability distribution. The occurrence probability was calculated every 25 m/s for 9 velocity thresholds. The same analysis was performed for SHF in Figure 2a. While the peak of the distribution for all data points was found close to zero velocity error (at −25 m/s more precisely), the probability distribution for SECS was more sharply peaked with nearly twice as high probability at the peak, indicating a higher accuracy of the 2-D flow velocity than SHF. The velocity error at the peak of the distribution reduced from −375 (SHF) to −200 m/s (SECS) for >500 m/s flows, and from −575 m/s (SHF) to −350 m/s (SECS) for >800 m/s flows. The occurrence of moderate-to-large velocity errors (<–400 and >300 m/s) decreased by a factor of 3.

Figures 2c and 2d show velocity errors in percentage (velocity error normalized by the LOS velocity). The SHF velocity error peaked at 65%, while the peak of the SECS velocity error was significantly lower (35%) for all levels of flow strengths. The occurrence of large (<−100% and >100%) velocity errors also reduced by 30%. These comparisons demonstrate that SECS provides flows that are fairly consistent with the measured LOS velocity. This improvement was achieved by removing the use of spherical harmonic functions and background convection models, as well as by increasing the spatial resolution. On the other hand, a notable level of velocity error is still present in SECS for multiple reasons: Even if ionospheric convection is perfectly divergence-free, the measured LOS velocity pattern may not exactly satisfy the divergence-free condition, because SuperDARN

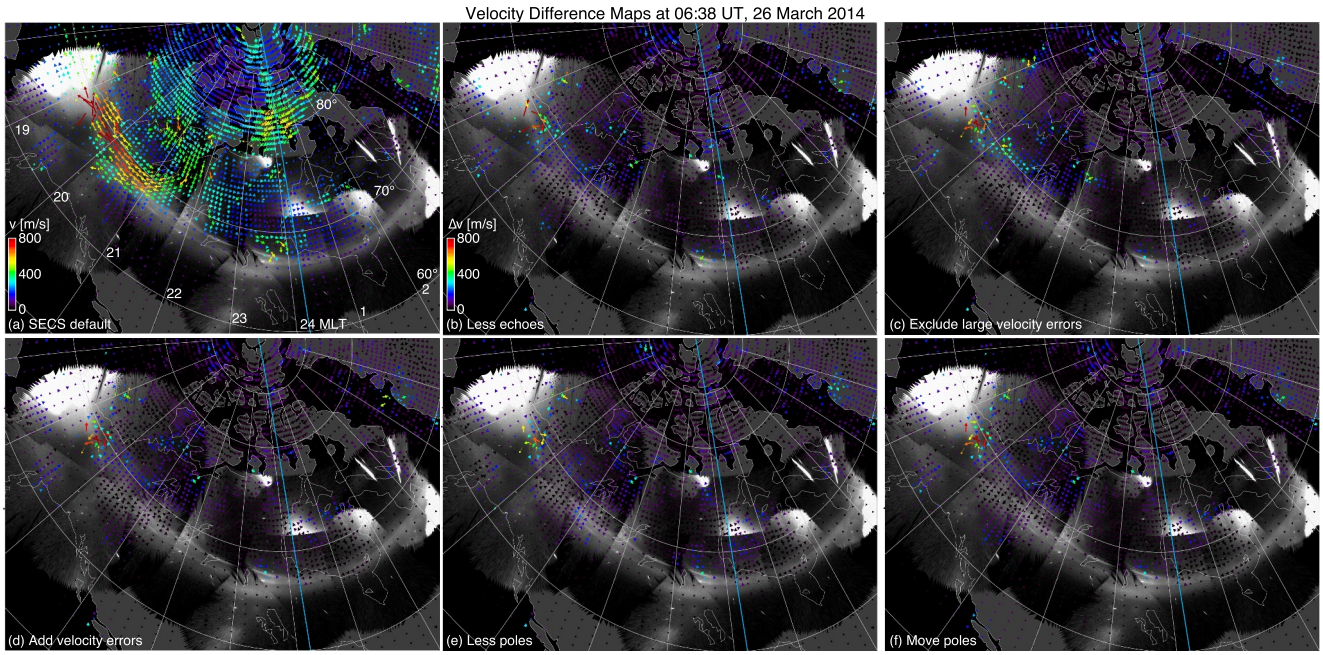

Figure 3. (a) Same as Figure 1c, denoted as the default spherical elementary current systems (SECS) map. Panels (b–f) show the SECS velocity distributions by (b) using less echoes, (c) excluding echoes with large LOS velocity errors, (d) adding or subtracting LOS velocity errors, (e) using less poles, and (f) moving poles randomly. Panels (b–f) subtracts the velocity in panel (a).

cannot resolve flow structures less than several tens of km and because flow variations faster than a few minutes cannot be measured either. The errors in LOS velocity measurements that are mentioned in Section 2.2 also distort convection patterns. The optimization by the SVD method attempts to filter out small-scale fluctuations that deviate from divergence-free flow patterns, and it acts as a low-pass filter and hence underestimates the velocity.

We also estimated uncertainties of 2-D flow vectors by performing five additional SECS runs by varying the model setup: (a) removing 10% of radar echoes randomly, (b) removing echoes that had >50% errors of LOS velocity, (c) adding or subtracting LOS velocity errors randomly, (d) removing 10% of poles randomly, and (e) moving poles by <100 km randomly. These runs intended to test how sensitive the SECS 2-D convection maps are to (a) the echo coverage, (b) LOS data points with large errors, (c) LOS velocity errors, (d) the number of poles, and (e) pole locations. The measurement errors of the LOS velocities were obtained from the radar data files.

Figure 3 shows convection maps for the default and five additional runs at 06:38 UT on 26 March 2014. Figure 3a is the map for the default setup, identical to Figure 1d. This map was subtracted from the maps for runs (a) through (e), and the velocity differences are presented in Figures 3b–3f. The velocity differences in Figures 3b–3f are small overall, indicating that much of the convection pattern in Figure 3a is robust and does not depend strongly on small variations of the model setup. The largest velocity differences were found in Northern Alaska, where the dense echo region with large LOS velocity was adjacent to the region of sparse and small LOS velocity (Figure 1a). The ambiguities about how the fast westward flow should continue farther duskward increased the uncertainties. Moderate velocity differences of ∼400 m/s were found in isolated regions where the echoes were sparse and were expected to have uncertainties. Where dense echo coverage existed, velocity differences were less than ∼100 m/s.

The SECS convection maps for runs (a) through (e) were created every 2 min at 5–10 UT on 26 March 2014. The velocity differences from the default run were calculated in the same manner as in Figure 3 at each UT. We combined all velocity differences and calculated occurrence probability distributions of the velocity magnitude differences (Figure 4a) and angle differences (Figure 4b). The distributions sharply peaked around zero. The median errors were as small as 22 m/s and 3°. The small errors confirm that the convection maps were obtained reliably without strong dependence on the model setup.

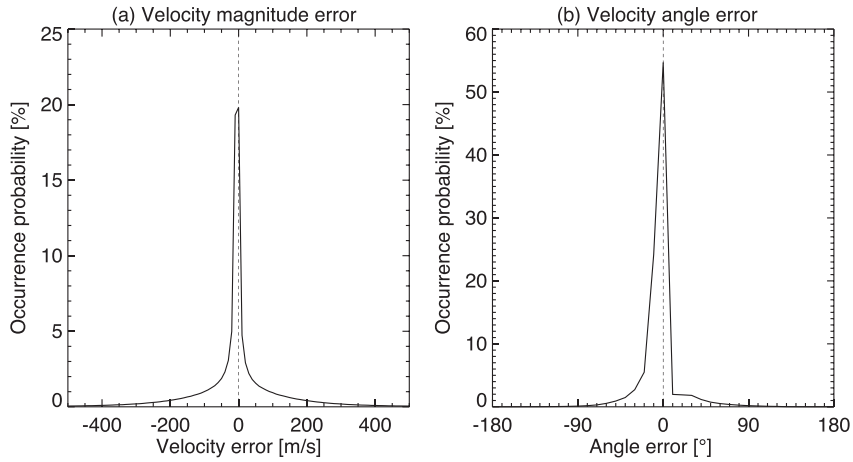

Figure 4. Occurrence probability distributions of the (a) velocity magnitude error and (b) velocity angle error. Here the velocity error is defined as the velocity differences in Figures 3b–3f but using all data points at 5–10 UT.

3.2. Validation With DMSP

The trajectory of DMSP-17 at 07:44-07:51 UT mapped from the southern hemisphere is shown in Figures 5a and 5b as a white line, overlaid onto the SHF and SECS convection maps at 07:48 UT. We chose this satellite path to compare the measured cross-track velocity and the 2-D flow vectors projected to the cross-track direction, because the cross-track direction was reasonably close to the 2-D flow vectors. The radar echoes were present in much of western Alaska (indicated as thick vectors) in the vicinity of the satellite path, and the 2-D flow vectors around the satellite track were mostly directed westward and northwestward. Although we did not anticipate a precise agreement between DMSP and SuperDARN because of the observations in the different hemispheres, we evaluated how much the flow structures in SHF and SECS represent the in situ observations.

The DMSP cross-track velocity was enhanced sunward at 61°–68° MLAT with a narrow peak at 66°–68° MLAT and anti-sunward weakly at >68° MLAT (Figure 5c). The cross-track SHF and SECS velocities successfully

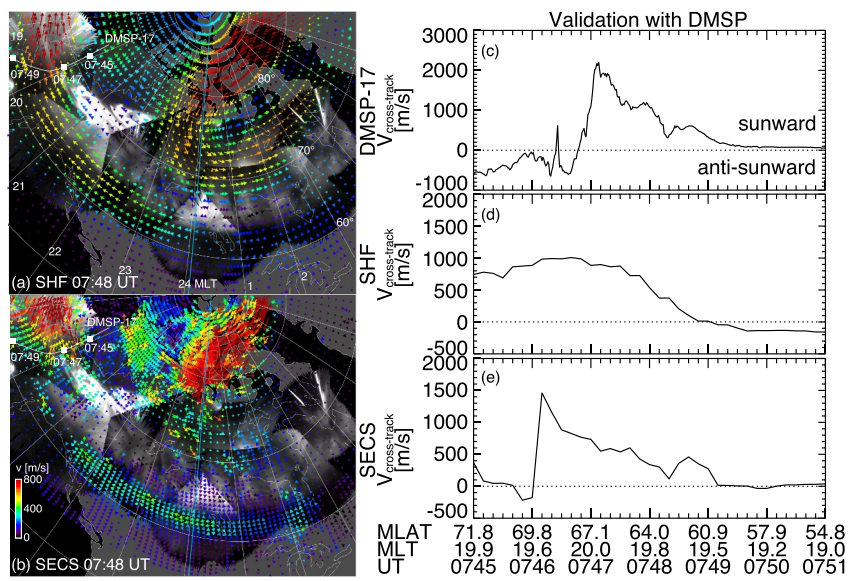

Figure 5. Validation with Defense Meteorological Satellite Program (DMSP) observations. (a) Spherical harmonic fit (SHF) and (b) spherical elementary current systems (SECS) velocity maps at 07:48 UT. The white line shows the DMSP-17 satellite track mapped to the northern hemisphere using the Tsyganenko (2002) magnetic field model. (c) Cross-track velocity measured by DMSP-17, positive sunward. (d) SHF and (e) SECS velocities projected to the cross-track direction at the spatial grid and UT nearest to each DMSP data point.

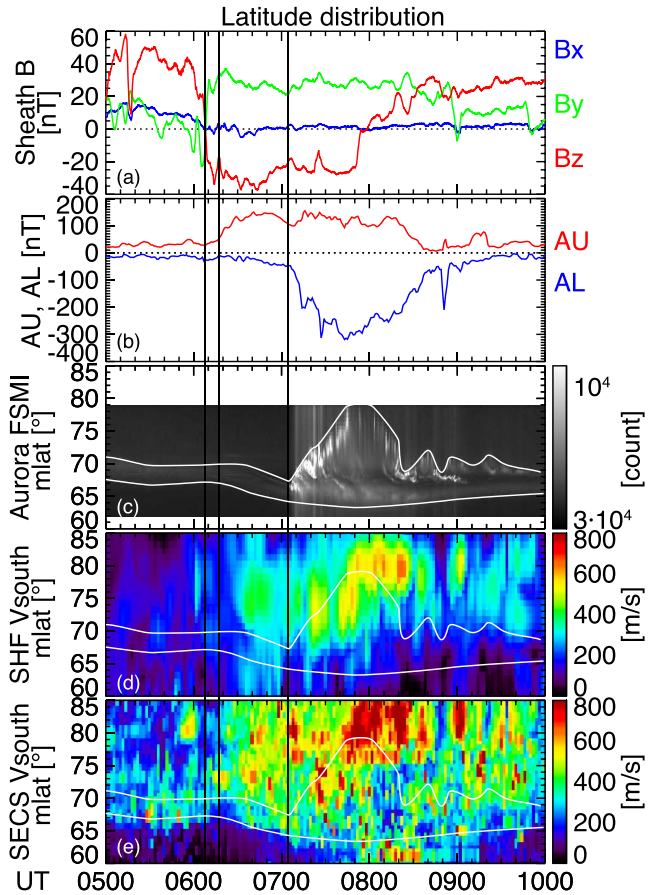

Figure 6. (a) Magnetosheath magnetic field from THEMIS-A near the subsolar magnetopause at $(X, Y) = (10.3, -3.2)$ R_E. (b) *AU* and *AL* indices. North-south keograms of (c) THEMIS ASI data at FSMI near midnight, (d) spherical harmonic fit maximum equatorward velocity at 20–3 hr MLT, and (e) spherical elementary current systems maximum equatorward velocity at 20–3 hr MLT. The white lines visually trace the poleward and equatorward boundaries of the auroral oval as the poleward-most and equatorward-most emissions except for the polar cap arcs.

reproduced the equatorward boundary of the enhanced sunward velocity. SHF only showed a broad westward velocity. Its poleward boundary extended beyond 72° MLAT, and the SHF flow was smooth and did not exhibit any localized structure. The peak SHF velocity was about 45% of the DMSP measurement, a large underestimation of the velocity. In contrast, the cross-track velocity from SECS reconstructed multiple peaks. The narrow velocity peak of ∼2° latitudinal width was reproduced successfully, although the peak velocity was underestimated (∼70% of DMSP) and the flow reversal latitude was shifted poleward by ∼2°. SECS also reconstructed the secondary peaks of the sunward velocity at 63° and 65°. Considering that SuperDARN tends to underestimate the flow velocity by ∼25% (Koustov et al., 2016) and to have echo location uncertainties of ∼100 km (Yeoman et al., 2008), SECS gave a good agreement with DMSP, demonstrating its capability to provide realistic high-resolution convection maps.

3.3. Flow Evolution During the Substorm: Latitudinal and Local Time Distributions

We utilized the SECS convection maps to describe the evolution of flow structures during the 26 March 2014 substorm. We show that the magneto-sheath magnetic field near the subsolar magnetopause was measured by THEMIS-A (Figure 6a), since observations near the subsolar magnetopause provided a better estimate of the arrival of IMF orientation changes than observations in the solar wind. The IMF turned southward and duskward at 06:08 UT. The IMF B_z was directed northward for several hours prior to the IMF southward turning. The *AU* index started to rise (Figure 6b), and the auroral oval started to move equatorward at 06:18 UT (Figure 6c), indicating the initiation of the substorm growth phase upon the signal arrival of the IMF southward turning to the ionosphere. Substorm auroral onset occurred at 07:05 UT (Figure 6c), followed by poleward expansion and numerous in-tensifications occurred along the poleward expanding arc (expansion phase). The IMF B_z turned northward at ∼07:50 UT, and then the substorm activity slowly decayed over time (recovery phase).

Figures 6d and 6e present the latitudinal distributions of the maximum equatorward velocity at 20-3 hr MLT for SHF and SECS. The equatorward component was chosen for visualizing how flows extend from the polar cap to the auroral and mid-latitudes. The convection maps below show the 2-D flow pattern. The poleward and equatorward boundaries of the auroral oval at Fort Smith (FSMI) as a representative station near midnight were traced visually (Figure 6c) and were copied to these panels. For both SHF and SECS, the equatorward velocity was enhanced during the substorm growth phase. The SECS flow enhancement above 80° MLAT initiated around 06:18 UT, in agreement with the initiation of the *AU* enhancement. Since SECS does not depend on a background convection map, the timing agreement with *AU* serves as validation of the technique to reproduce the time variation of the convection. The SHF convection in the polar cap was enhanced after 06:20 UT, and it coincided with the IMF southward turning in the OMNI data (not shown). Because the background convection in SHF is parameterized by the IMF, the timing error in OMNI has a measurable impact on the convection map.

The enhanced convection in the polar cap extended toward lower latitudes and penetrated to the auroral oval by ∼06:40 UT. The poleward boundary of the auroral oval was not clearly defined until ∼06:30 UT, but then an auroral arc formed at the poleward boundary and moved equatorward. The formation of the poleward boundary arc coincided with the arrival of the enhanced flows at the oval poleward boundary, and it is likely due to weak magnetotail reconnection driven by the enhanced flows crossing the open-closed boundary.

The flows increased during the substorm expansion and early recovery phases (07:05–08:30 UT), and the enhanced flows crossed the poleward boundary of the auroral oval repetitively. The flow across the poleward

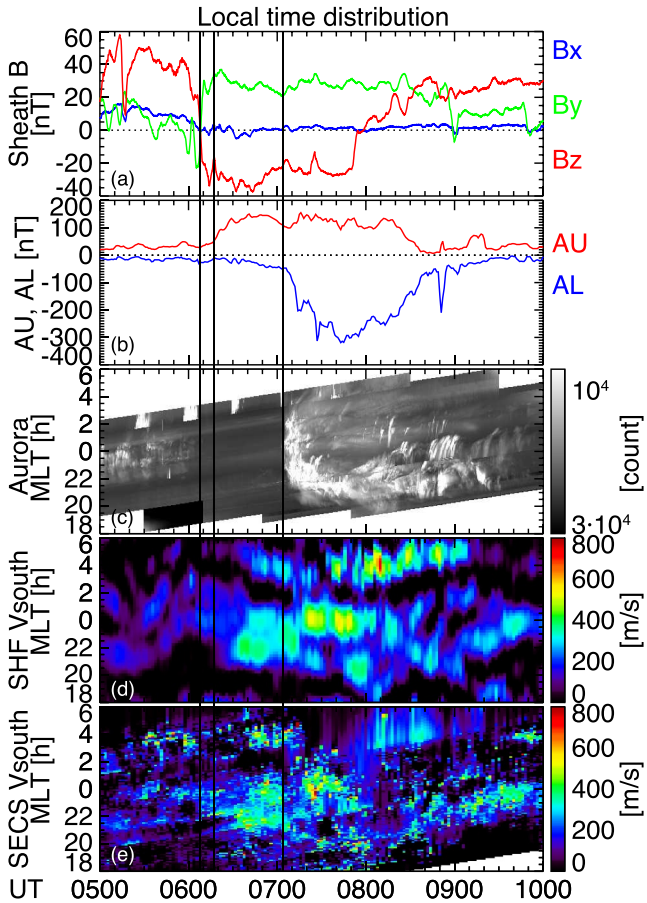

Figure 7. (a–b) Same as Figures 6a and 6b. East-west keograms of (c) maximum THEMIS ASI intensify at each MLT, (d) spherical harmonic fit maximum equatorward velocity at each MLT at 68°–73° MLAT, and (e) spherical elementary current systems maximum equatorward velocity.

boundary is the ionospheric signature of magnetotail reconnection, where flux tubes in the lobe are transported to the plasma sheet through the open-closed boundary. Individual flow enhancements lasted for ~10 min, which are likely the ionospheric counterpart of flow bursts in the plasma sheet. The flows generally decreased as they extended equatorward but reached the equatorward boundary of the auroral oval and even to the subauroral ionosphere. The SHF velocity changed more smoothly and significantly underestimated the rapid variation. As shown in Figure 1, SECS has a better capability to resolve localized flows, which tend to vary rapidly. In addition, the fast variations of the flows do not correlate with the IMF, and thus techniques that use IMF-dependent background convection models tend to underestimate such rapid variations.

The flows in the auroral oval decreased during the recovery phase after 8 UT, while the polar cap flows increased at ~07:50 UT and remained fast until ~08:26 UT. The enhanced polar cap flows with weak flows in the auroral oval may have contributed to the equatorward motion of the oval poleward boundary. This period also corresponded to enhanced subauroral flows. As shown later, this is related to westward-directed SAPS flows, where its small equatorward component is seen in this panel. The polar cap flows weakened in the late recovery phase (after 08:30 UT), while flows in the equatorward portion of the auroral oval diminished more rapidly.

Figure 7 compares the MLT distribution of aurora and the maximum equatorward flows at 68°–72° MLAT. For both SHF and SECS, the flow speed increased gradually at pre-midnight during the growth phase at ~21–1 and ~3–5 hr MLT. The initial brightening of the auroral substorm was located near midnight and spread quickly to ~22–2 hr MLT within a few minutes from the substorm onset (Figure 7c), almost overlapping the ~21–1 hr MLT flow (Figures 7d and 7e). It is reasonable to expect this relation, because the flows in the growth phase drive the plasma sheet thinning and the plasma sheet becomes more unstable in the region of the stretched tail current sheet (Pritchett & Lu, 2018). The flows at ~3–5 hr MLT were not involved in the substorm onset, but the auroral brightening spread dawnward to >4 hr MLT during the expansion phase. The duskward boundary of the bright aurora expanded duskward to ~21 hr MLT and became the brightest part of the aurora (westward traveling surge), while the aurora dawnward of the surge weakened. Flows during the expansion phase were the fastest and localized near midnight with transient enhancements. In SECS, the region of enhanced flows extended duskward until ~08:00 UT in a similar manner to the motion of the surge. In contrast, the flows at post-midnight decreased after ~07:20 UT and the flow reduction extended duskward. The flow reduction after onset was also seen in statistical results of SHF (Grocott et al., 2009). After ~08:00 UT, the auroral surge weakened but moderate auroral activity spread at ~21–2 hr MLT with dawnward propagation. The SECS flows also moved dawnward, and the peak of the enhanced flows retuned to midnight. The SHF flows also shifted duskward and then dawnward, but with less MLT motion. The SHF flows near midnight remained during the expansion phase even though aurora near midnight weakened considerably.

SHF found multiple flow channels at each time, each of which had a ~2–4 hr MLT width. SECS detected narrower and larger peaks that were highly variable. Such meso-scale flow channels were particularly evident during the expansion and early recovery phases (e.g., near midnight at 07:20–07:30 UT), but they were also present in the quiet time before 6 UT.

3.4. Flow Evolution During the Substorm: 2-D Convection Maps

Representative SECS convection maps before the substorm onset are depicted in Figure 8. Overall, the flow and aurora were weak during the quiet time (Figure 8a). The large-scale two-cell convection was essentially absent, and the flow structure was dominated by weak flow channels that are indicated by the white arrows. After the IMF

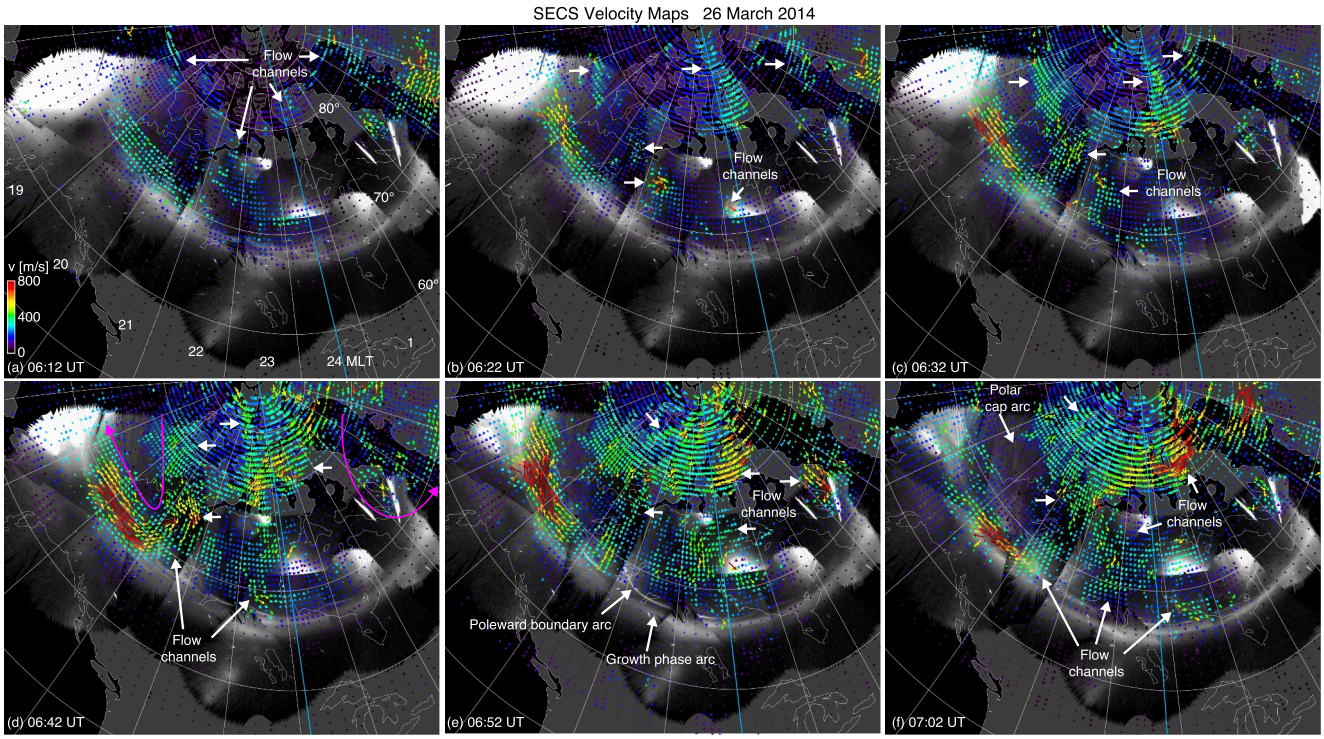

Figure 8. Selected maps of the spherical elementary current systems velocity before and during the growth phase of the substorm.

southward turning, the flow speed increased deep in the polar cap near the magnetic pole and in the duskside auroral oval, while the flows around the auroral oval near midnight remained weak (Figure 8b). The convection pattern was still mainly characterized by the flow channels with minimal large-scale convection. Then the equatorward flow channels extended from deep in the polar cap toward the pre-midnight auroral oval (Figure 8c). Flow channels in the polar cap merged and bifurcated along the streamlines, indicating dynamic interaction between the flow channels, and the auroral oval started to move equatorward as the enhanced flows reached the oval (Figure 6). The flow speed continued to increase, and the enhanced flows extended more equatorward and azimuthally (Figures 8d–8f). The large-scale two-cell pattern became evident by these times as indicated by magenta lines in Figure 8d, but many flow channels were clearly present (Figure 7). The flows above ∼75° MLAT extended from post-midnight toward pre-midnight, whose orientation is consistent with a convection pattern under a positive IMF B_y (Figure 6a). Flows below ∼75° MLAT down to the auroral oval were almost north-south oriented, exhibiting less influence of the IMF B_y. Grocott et al. (2010) also noted that the IMF B_y effects are prominent in the polar cap, but that convection in the nightside oval is more related to the onset location.

Interestingly, the flow channels were connected from deep in the polar cap to the vicinity of the nightside auroral oval and then toward the dusk or post-midnight almost continuously. The connection over the long extent was seen for ∼30 min during the growth phase, but the flow channel paths dynamically changed in several minutes, also exhibiting merging and bifurcation. Equatorward flows near the poleward boundary of the auroral oval near the end of the growth phase were confined between ∼21 and ∼1 hr MLT (Figures 8e and 8f). The auroral oval moved more equatorward in this local time sector, indicating that the plasma sheet at pre-midnight became thinner than in the other regions due to the stronger convection electric field (stronger loading). The flows in this region were not uniform but had localized peaks at 21.5 and 23 and 0.5 hr MLT. A polar cap arc was present at the center of the clockwise flow shear (Figure 8f), which validates that SECS reasonably identified the flow shear location.

The substorm onset occurred near midnight around the dawnward edge of the enhanced equatorward flows (Figure 9a). The flow channel at ∼0.5 hr MLT during the growth phase could be the precursor flows for driving the substorm onset (Bristow et al., 2003; Lyons et al., 2022; Nishimura, Lyons, Zou, Angelopoulos, & Mende, 2010). As seen in Figure 9a, the initial brightening in the first few minutes from onset extended over a large portion of the equatorward flows (∼22–1 hr MLT), showing the connection between the growth-phase flow

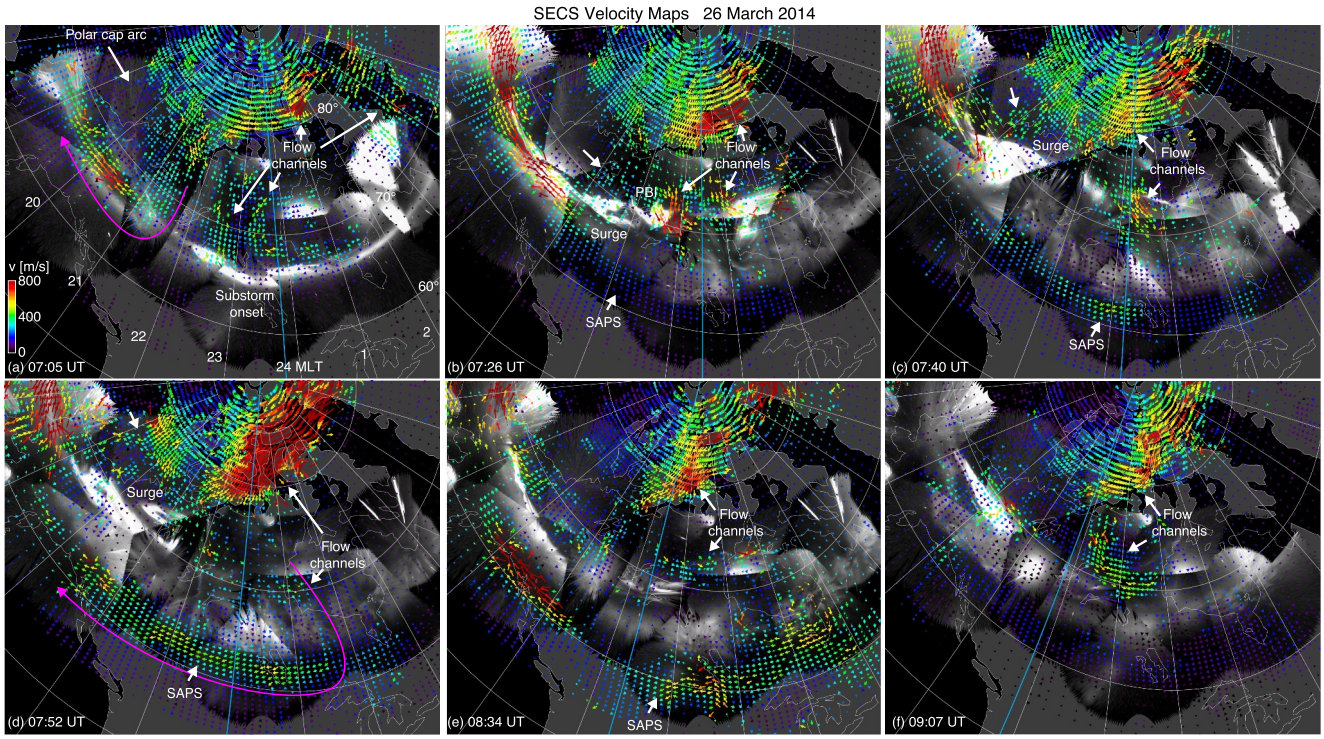

Figure 9. Selected maps of the spherical elementary current systems velocity during the expansion and recovery phases of the substorm. The magenta lines illustrate the Harang flow shear.

pattern and substorm onset. The onset location was found near the separator between the duskside and dawnside convection cells. The main Harang flow shear was located before 21.5 hr MLT slightly poleward of the growth phase arc, and the onset location was well to the east of this flow shear. Regarding the relation between the Harang and onset (Bristow, 2009; Zou et al., 2013), this onset was either equatorward of the Harang or unrelated to the Harang.

The auroral breakup during the early expansion phase quickly spread over 22–2 hr MLT (Figure 9b), whose extent is likely related to the local time range of the equatorward flows (stronger loading) during the growth phase. The most notable feature in Figure 9b is the localized and fast flow channel with a ∼0.3 hr MLT width at ∼23.5 hr MLT. It was located to the east of a localized discrete auroral brightening at the auroral poleward boundary (PBI), where a flow channel is expected (Nishimura et al., 2011). This is likely the ionospheric projection of a flow burst in the plasma sheet, and SECS was able to reconstruct its 2-D structure. The flow channel appears to be crossing from the polar cap into the auroral oval, representing localized magnetotail reconnection (de la Beaujardiere et al., 1994), although its full north-south extent could not be determined due to the lack of echoes farther to the north. The flow channel had a southeastward orientation as opposed to the southwestward flows deep in the polar cap. The flow channel weakened as it extended equatorward but reached the equatorward boundary of the auroral oval. It contributed to the enhanced westward flows equatorward of the auroral oval. This westward flow enhancement is consistent with the rapid response of SAPS during substorms (Mishin et al., 2017; Nishimura et al., 2008), and this convection map provided a 2-D picture of the direct impact of plasma sheet flow bursts on SAPS. The SAPS flow speed was low at the time of Figure 9b, and much of the westward flows were mainly in the auroral oval as can be seen at <21 hr MLT. Another localized flow channel was seen at ∼1 hr MLT, and it turned eastward as it entered the auroral oval.

The localized flow channels appeared repetitively during the substorm. Another example is shown in Figure 9c. The flow channel near midnight was located just to the east of a PBI and streamer, similar to the one in Figure 9b, and appeared to have entered the oval from the polar cap. The flows in the nightside auroral oval decreased overall, but this flow channel turned eastward and then equatorward, forming a developed Harang flow shear, as the enhanced flows reached the subauroral ionosphere and further enhanced the SAPS flow. Flows at ∼22–24 hr

MLT in the auroral oval were reduced overall, and the enhanced flows from the polar cap bifurcated to two flow structures, one toward the surge head at ~21–22 hr MLT and the other toward the Harang flow shear at >23 hr MLT.

The surge weakened near the end of the expansion phase (Figure 9d). The polar cap flows toward the surge head split to multiple channels and shifted further duskward. The polar cap flows showed a localized enhancement near midnight, and most flows were directed toward post-midnight around the Harang flow shear and SAPS, although the flow speed at post-midnight decreased. Fast equatorward flow channels in the auroral oval disappeared, and instead the oval poleward boundary started to move equatorward (Figure 6). In the recovery phase, the surge and active aurora almost disappeared (Figure 9e). The polar cap flows weakened particularly at pre-midnight. Flows near midnight were more aligned with the poleward boundary, and the region of the equatorward turning shifted to post-midnight after 3 hr MLT, although its details were unknown due to the lack of echoes. Much of the polar cap flows entered the auroral oval from post-midnight, and SAPS flows were at their maximum strength. Flows weakened further and were confined near midnight in the late recovery phase, and fewer flows entered the auroral oval (Figure 9f). The flow channel still maintained the connection from deep in the polar cap to the poleward boundary of the auroral oval, while fewer flows extended toward the auroral oval and subauroral ionosphere.

3.5. Quantifying Meso-Scale Flow Contributions

To assess the impact of the meso-scale flow channels, we quantified the contribution of these flow channels to the total transport in the nightside high-latitude ionosphere. By inspecting Figures 8 and 9, Figure 7d adequately represents the meso-scale flow structures near the poleward boundary of the auroral oval. The data (copied as Figure 10b) were decomposed to large-scale and meso-scale components with azimuthal size thresholds of 0.3, 1.0, and 2.0 hr MLT (~180, 600, and 1,200 km at 70° MLAT). We considered the three representative scales, because the choice of the threshold could affect how much of the localized transport was classified as meso-scale.

The large-scale and meso-scale flows for a 2.0 hr MLT cut-off are shown in Figures 10c and 10d. The large-scale component identified a broad equatorward flow of >~3 hr MLT width that was centered at pre-midnight to midnight, and an additional large-scale equatorward flow was occasionally seen at post-midnight (Figures 8a, 8d, and 9a). This large-scale flow structure was overall in agreement with the SHF convection in Figure 7e. The meso-scale flows reasonably extracted the localized flow enhancements seen in Figure 10b. Each meso-scale flow had a width of a fraction of hours in MLT and lasted several minutes. Multiple flow channels could appear simultaneously. The meso-scale flows after the substorm onset were mainly observed in the region of enhanced large-scale flows, while the meso-scale flows during the quiet time and growth phase could appeared outside the large-scale flows.

The mean equatorward velocity is shown in Figure 10e. This plot confirms the large-scale flow enhancement during the growth and early recovery phases (~06:18–09:00 UT). Figure 10f quantifies the contribution of the meso-scale equatorward transport to the total equatorward transport in the nightside high-latitude ionosphere. The total and meso-scale equatorward transports were obtained by integrating data in Figures 10b and 10d along MLT, respectively. The meso-scale transport contributions were on average 33% (<2 hr MLT), 23% (<1 hr MLT), and 10% (<0.3 hr MLT) of the total transport. However, meso-scale contributions were highly variable. The meso-scale contributions were the highest during the quiet time and recovery phase, where the large-scale convection was weak. The meso-scale transport strengths did not scale with the large-scale transport strength, but fast meso-scale flows were present throughout this time interval. The average meso-scale contributions for those times were 43% (<2 hr MLT), 29% (<1 hr MLT), and 12% (<0.3 hr MLT). Each meso-scale flow structure only lasted for several minutes, resulting in numerous spikes in the meso-scale contributions across all spatial scales. The highest values reached 73% (<2 hr MLT), 45% (<1 hr MLT), and 28% (<0.3 hr MLT). The meso-scale contributions decreased with increasing large-scale transport during the growth and expansion phases, but the meso-scale transport continued to carry a significant portion of the convection (with averages of 26% (<2 hr MLT), 20% (<1 hr MLT), and 9% (<0.3 hr MLT)). The meso-scale transport during the active aurora was also highly variable.

Multiple meso-scale flow structures were seen at each time in general, and thus the meso-scale contributions counted the sum of the multiple flow channels. The contribution of a single flow channel could only be evaluated for short times at 07:00 and 09:56 UT, when a single flow channel dominated the meso-scale flow pattern. The contribution of the single flow channel was 27% (<2 hr MLT), 15% (<1 hr MLT), and 6% (<0.3 hr MLT) (07:00

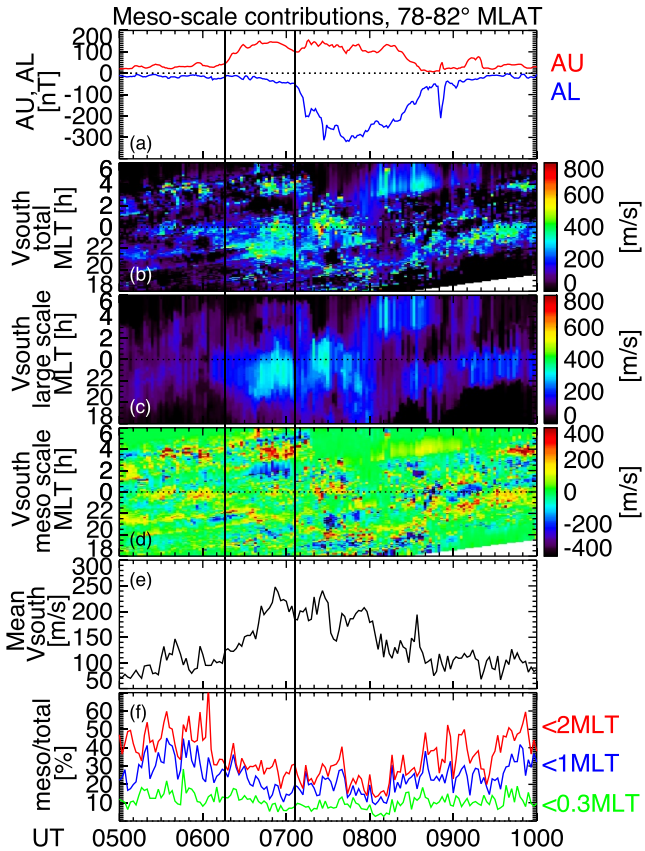

Figure 10. Evaluation of meso-scale flow contributions around the poleward boundary of the auroral oval (78°–82° MLAT). (a) *AU* and *AL* indices, (b) same as Figure 7d, (c) same as panel (b) but smoothed over 1,000 km (large-scale velocity). (d) Difference between Panels b and c (meso-scale velocity). (e) spherical elementary current systems equatorward velocity averaged over 20-4 hr MLT. (f) Contributions of meso-scale velocity relative to the total velocity for three thresholds of the meso-scale velocity.

UT, strong large-scale flows), and 37% (<2 hr MLT), 29% (<1 hr MLT), and 10% (<0.3 hr MLT) (09:56 UT, weak large-scale flows). These values are somewhat lower than but comparable to the averaged values mentioned above, because the flow channel was relatively strong. The contribution of a weak flow channel would certainly be smaller, although there was no time instance in this event, when a single weak flow channel was present. A few tens of percent of meso-scale contributions are consistent with the contributions of bubble injections in the magnetotail (Gkioulidou et al., 2014; Yang et al., 2015).

The same analysis was performed for polar cap flows at 82°–84° MLAT (Figure 11). The 0.3, 1.0 and 2.0 hr MLT thresholds correspond to ~60, 200 and 400 km at 83° MLAT. Since the flow vectors were tilted to the southwest after ~06:40 UT (Figures 7 and 8), the equatorward component is less than the total flow speed, and the MLT flow width tends to be wider than the width perpendicular to the flows. However, it is difficult to change the cross section dynamically, and thus we used the cut along the constant latitude as a proxy for the flow structure. The flow structure was smoother and more dominated by large-scale flows (Figure 11b) than in the auroral oval. The large-scale flows started to increase at post-midnight at ~06:18 UT and moved to pre-midnight (Figure 11c). Unlike classical two-cell convection, two regions of enhanced flows characterized the polar cap flow structure after ~06:30 UT. After the substorm onset, the polar cap flows stopped moving westward and turned back toward post-midnight. The flow speed increased in the early recovery phase (07:50–08:20 UT), and then became weaker and intermittent. Flows in the recovery phase were predominantly located at post-midnight.

Numerous meso-scale flows were observed, each with ~1 hr MLT widths, and they lasted for several minutes (Figure 11d). The meso-scale flows were located predominantly at post-midnight in the region of the large-scale flows. This represents a significant difference from Figure 10d, where the meso-scale flows were distributed across a wider range of MLT and were more frequent at pre-midnight during the expansion and early recovery phases. Similar to Figure 10f, the meso-scale flows made the largest contributions in the quiet time before 06:18 UT (with averages of 26% (<2 hr MLT), 15% (<1 hr MLT), and 5% (<0.3 hr MLT)). The meso-scale contributions decreased once the growth phase started (with averages of 16% (<2 hr MLT), 10% (<1 hr MLT), and 3% (<0.3 hr MLT)). In contrast to Figure 10f, the meso-scale contributions increased only slightly during the recovery phase. The lower contributions and MLT asymmetry of the meso-scale flow channels in the polar cap suggest that the meso-scale flow channels around the poleward boundary of the auroral oval were not simply imposed from the polar cap but also originated from plasma sheet processes, such as magnetotail configuration, magnetotail reconnection and plasma sheet flow bursts. Nevertheless, the maximum meso-scale contribution was substantial, reaching 68% during the quiet time.

The transient enhancements corresponded to enhancements of the flow channels. The spatially isolated flow channel observed at 08:56 UT illustrates that a single flow channel can contribute significantly to the total convection, with averages of 19% (<2 hr MLT), 10% (<1 hr MLT), and 3% (<0.3 hr MLT).

4. Summary and Conclusion

We have developed and evaluated an approach for creating continental-scale, high-resolution plasma convection maps using the SECS technique. This approach was applied to examine high-resolution 2-D plasma convection in the nightside high-latitude ionosphere during a substorm event. We demonstrated that this approach can reconstruct convection maps that retain the meso-scale flow structures. The comparison with the LOS velocity showed that the SECS velocity substantially improved accuracy compared to SHF. The peak occurrence of the velocity error was 35%, a significant reduction from the 65% error for SHF. The occurrence of large velocity errors also reduced by 30%. High accuracy was achieved by removing background convection models and

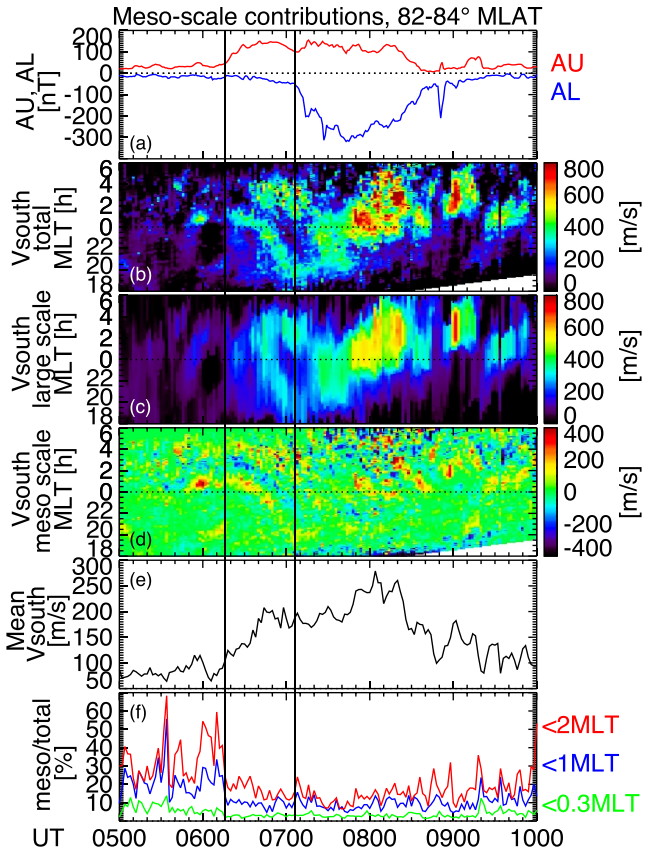

Figure 11. (a–b) Same as Figure 10 but for flows in the polar cap (82°–84° MLAT).

increasing spatial resolution. The SECS convection maps were not sensitive to the model setup (22 m/s and 3° median uncertainties), providing robust flow structures. Validation with DMSP demonstrated that SECS is capable of reconstructing realistic flow structures.

We demonstrated the value of the SECS convection maps for evaluating the relation between meso-scale flows and auroral structures by investigating the evolution of high-resolution flow structures during the substorm. The timing of the flow enhancement in the polar cap at the beginning of the growth phase was more accurate for SECS than SHF, because SECS is free from timing errors in the arrival of solar wind structures to Earth. Meso-scale flow channels dominated the convection pattern with minimal large-scale convection in the early growth phase. Multiple flow channels extended from the polar cap toward the nightside auroral oval, forming continuous flow channels over >20° of latitude. The flow channels dynamically merged and bifurcated, indicating an active interplay between the flow channels. The poleward boundary of the auroral oval illuminated as the flows reached the oval poleward boundary. Large-scale convection developed in the late growth phase, but the flow channels were still evident. The flows deep in the polar cap were tilted toward pre-midnight, while the flows near but poleward of the auroral oval were more north-south aligned. The enhanced flows near the oval poleward boundary were located at 21–1 hr MLT, where the auroral oval moved more equatorward than other MLT.

The substorm onset was located near the dawnward edge of the enhanced flows. The initial width of the auroral breakup coincided with the width of the enhanced flows, suggesting that the flow channels are the precursor flows to the substorm onset. During the substorm expansion phase, enhanced meso-scale flows crossed the oval poleward boundary near midnight repetitively, each of which had a ∼2–4 hr MLT width and ∼10 min duration. Some flows reached the oval equatorward boundary and subauroral ionosphere, contributing to enhance SAPS flows. The enhanced flows extended duskward as the auroral surge moved duskward. The polar cap flows toward the auroral oval split to the dusk and dawn of the surge. The flows turning dawnward formed a Harang flow shear and connected to the subauroral flows. Post-midnight flows decreased, and the flow reduction extended duskward. Weak to moderate flow and auroral activities returned to midnight during the recovery phase. The Harang flow shear became more pronounced, and the SAPS flow speed increased.

We further quantified the contributions of the meso-scale transport to the total transport in the nightside high-latitude ionosphere. The meso-scale contributions were the highest during the quiet time and recovery phase, where the large-scale convection was weak. Near the poleward boundary of the auroral oval, the meso-scale contributions were 12%–43% of the total transport (quiet time and recovery phase) and 9%–26% (growth and expansion phases) depending on the scale-size threshold. The meso-scale contribution was highly variable on a ∼10-min time scale due to the transient nature of the flow channels. The peak contribution reached 28%–73%. Multiple flow channels existed simultaneously for most times. The meso-scale contribution deep in the polar cap was ∼10%–20% lower, but substantial meso-scale flow structures still existed despite being far away from the auroral oval.

Data Availability Statement

The SuperDARN, THEMIS, DMSP, and AU/AL data are available at the corresponding project websites (Angelopoulos, 2008; Chartier, 2022; Papitashvili & King, 2020; Rideout, 1980). The SECS velocity vector output is available at Zenodo (Nishimura, 2024). Data processing used SPEDAS-V3.1 (Angelopoulos et al., 2019).

Acknowledgments
This work was supported by NASA Grants 80NSSC20K0725, 80NSSC21K1321, 80NSSC22K0323, 80NSSC22K0749, 80NSSC23M0193, 80NSSC23K0410, 80NSSC20K1314, 80GSFC22CA011 and 80NSSC23K1062, NSF Grants AGS-1907698, AGS-2055192 and AGS-2100975, and AFOSR Grants FA9550-23-1-0614 and FA9550-23-1-0634. THEMIS is supported by NASA NAS5-02099 and Canada Foundation for Innovation. We thank ISSI/ISSJ-BJ through ISSI International Team projects Auroral Research Coordination: Towards Internationalised Citizen Science (ARCTICS), Multi-Scale Magnetosphere-Ionosphere-Thermosphere Interaction, and Magnetotail Dipolarizations: Archimedes Force or Ideal Collapse? We also thank Brianna Nguyen for proofreading the text.

References

Amm, O., Grocott, A., Lester, M., & Yeoman, T. K. (2010). Local determination of ionospheric plasma convection from coherent scatter radar data using the SECS technique. *Journal of Geophysical Research*, *115*(A3), A03304. https://doi.org/10.1029/2009JA014832

Amm, O., & Viljanen, A. (1999). Ionospheric disturbance magnetic field continuation from the ground to the ionosphere using spherical elementary current systems. *Earth, Planets and Space*, *51*(6), 431–440. https://doi.org/10.1186/bf03352247

Angelopoulos, V. (2008). THEMIS satellite level 2 data and ASI level 1 data [Dataset]. *University of California*. Retrieved from https://themis.ssl.berkeley.edu/themisdata/tha/l2/

Angelopoulos, V., Cruse, P., Drozdov, A., Grimes, E. W., Hatzigeorgiu, N., King, D. A., et al. (2019). The Space Physics Environment Data Analysis System (SPEDAS). *Space Science Reviews*, *215*(1), 9. https://doi.org/10.1007/s11214-018-0576-4

Bristow, W. A. (2009). Relationship between substorm onset locations and nightside convection pattern features. *Journal of Geophysical Research*, *114*(A12), A12202. https://doi.org/10.1029/2009JA014576

Bristow, W. A., Lyons, L. R., Nishimura, Y., Shepherd, S. G., & Donovan, E. F. (2022). High-latitude plasma convection based on SuperDARN observations and the locally divergence free criterion. *Journal of Geophysical Research: Space Physics*, *127*(12), e2022JA030883. https://doi.org/10.1029/2022ja030883

Bristow, W. A., Sofko, G., Stenbaek-Nielsen, H. C., Wei, S., Lummerzheim, D., & Otto, A. (2003). Detailed analysis of substorm observations using SuperDARN, UVI, ground-based magnetometers, and all-sky imagers. *Journal of Geophysical Research*, *108*(A3), 1124. https://doi.org/10.1029/2002JA009242

Chartier, A. (2022). SuperDARN FITACF v2.5 and v3.0 data [Dataset]. *Johns Hopkins University*. Retrieved from https://superdarn.jhuapl.edu/download

Chisham, G., Lester, M., Milan, S. E., Freeman, M. P., Bristow, W. A., Grocott, A., et al. (2007). A decade of the Super Dual Auroral Radar Network (SuperDARN): Scientific achievements, new techniques and future directions. *Surveys in Geophysics*, *28*(1), 33–109. https://doi.org/10.1007/s10712-007-9017-8

Cowley, S. W. H. (2000). Magnetosphere-ionosphere interactions: A tutorial review. In S.-I. Ohtani, R. Fujii, M. Hesse, & R. L. Lysak (Eds.), *Magnetospheric current systems*.

de la Beaujardiere, O., Lyons, L. R., Ruohoniemi, J. M., Friis-Christensen, E., Danielsen, C., Rich, F. J., & Newell, P. T. (1994). Quiet-time intensifications along the poleward auroral boundary near midnight. *Journal of Geophysical Research*, *99*(A1), 287–298. https://doi.org/10.1029/93JA01947

Fan, J., & Ma, G. (2014). Characteristics of GPS positioning error with non-uniform pseudorange error. *GPS Solutions*, *18*(4), 615–623. https://doi.org/10.1007/s10291-013-0359-z

Ferdousi, B., Raeder, J., Zesta, E., Cramer, W., & Murphy, K. (2021). Association of auroral streamers and bursty bulk flows during different states of the magnetotail: A case study. *Journal of Geophysical Research: Space Physics*, *126*(9), e2021JA029329. https://doi.org/10.1029/2021ja029329

Gabrielse, C., Nishimura, Y., Lyons, L., Gallardo-Lacourt, B., Deng, Y., & Donovan, E. (2018). Statistical properties of mesoscale plasma flows in the nightside high-latitude ionosphere. *Journal of Geophysical Research: Space Physics*, *123*(8), 6798–6820. https://doi.org/10.1029/2018ja025440

Gallardo-Lacourt, B., Nishimura, Y., Lyons, L. R., Zou, S., Angelopoulos, V., Donovan, E., et al. (2014). Coordinated SuperDARN THEMIS ASI observations of mesoscale flow bursts associated with auroral streamers. *Journal of Geophysical Research: Space Physics*, *119*(1), 142–150. https://doi.org/10.1002/2013ja019245

Gillies, R. G., Perry, G. W., Koustov, A. V., Varney, R. H., Reimer, A. S., Spanswick, E., et al. (2018). Large-scale comparison of polar cap ionospheric velocities measured by RISR-C, RISR-N, and SuperDARN. *Radio Science*, *53*(5), 624–639. https://doi.org/10.1029/2017rs006435

Gkioulidou, M., Ukhorskiy, A. Y., Mitchell, D. G., Sotirelis, T., Mauk, B. H., & Lanzerotti, L. J. (2014). The role of small-scale ion injections in the buildup of Earth's ring current pressure: Van Allen Probes observations of the 17 March 2013 storm. *Journal of Geophysical Research: Space Physics*, *119*(9), 7327–7342. https://doi.org/10.1002/2014JA020096

Grocott, A., Milan, S. E., Yeoman, T. K., Sato, N., Yukimatu, A. S., & Wild, J. A. (2010). Superposed epoch analysis of the ionospheric convection evolution during substorms: IMF BY dependence. *Journal of Geophysical Research*, *115*(A5), A00I06. https://doi.org/10.1029/2010JA015728

Grocott, A., Wild, J. A., Milan, S. E., & Yeoman, T. K. (2009). Superposed epoch analysis of the ionospheric convection evolution during substorms: Onset latitude dependence. *Annales Geophysicae*, *27*(2), 591–600. https://doi.org/10.5194/angeo-27-591-2009

Heppner, J. P., & Maynard, N. C. (1987). Empirical high-latitude electric field models. *Journal of Geophysical Research*, *92*(A5), 4467–4489. https://doi.org/10.1029/JA092iA05p04467

Koustov, A. V., Lavoie, D. B., & Varney, R. H. (2016). On the consistency of the SuperDARN radar velocity and $E \times B$ plasma drift. *Radio Science*, *51*(11), 1792–1805. https://doi.org/10.1002/2016RS006134

Laundal, K. M., Reistad, J. P., Hatch, S. M., Madelaire, M., Walker, S., Hovland, A. Ø., et al. (2022). Local mapping of polar ionospheric electrodynamics. *Journal of Geophysical Research: Space Physics*, *127*(5), e2022JA030356. https://doi.org/10.1029/2022ja030356

Lyons, L., Nishimura, Y., Liu, J., Zou, Y., Bristow, W. A., Yadav, S., et al. (2016). Unsolved problems: MesoScale polar cap flow channels' structure, propagation, and effects on space weather disturbances. *Journal of Geophysical Research: Space Physics*, *121*(4), 3347–3352. https://doi.org/10.1002/2016JA022437

Lyons, L. R., Nishimura, Y., Liu, J., Bristow, W. A., Zou, Y., & Donovan, E. F. (2022). Verification of substorm onset from intruding flow channels with high-resolution SuperDARN radar flow maps. *Journal of Geophysical Research: Space Physics*, *127*(8), e2022JA030723. https://doi.org/10.1029/2022ja030723

Lyons, L. R., Nishimura, Y., Zhang, S.-R., Coster, A. J., Bhatt, A., Kendall, E., & Deng, Y. (2019). Identification of auroral zone activity driving large-scale traveling ionospheric disturbances. *Journal of Geophysical Research: Space Physics*, *124*(1), 700–714. https://doi.org/10.1029/2018ja025980

Makarevich, R. A., & Dyson, P. L. (2007). Dual HF radar study of the subauroral polarization stream. *Annales Geophysicae*, *25*(12), 2579–2591. https://doi.org/10.5194/angeo-25-2579-2007

Mende, S. B., Harris, S. E., Frey, H. U., Angelopoulos, V., Russell, C. T., Donovan, E., et al. (2008). The THEMIS array of ground-based observatories for the study of auroral substorms. *Space Science Reviews*, *141*(1–4), 357–387. https://doi.org/10.1007/s11214-008-9380-x

Mishin, E., Nishimura, Y., & Foster, J. (2017). SAPS/SAID revisited: A causal relation to the substorm current wedge. *Journal of Geophysical Research: Space Physics*, *122*(8), 8516–8535. https://doi.org/10.1002/2017JA024263

Nicolls, M. J., Cosgrove, R., & Bahcivan, H. (2014). Estimating the vector electric field using monostatic, multibeam incoherent scatter radar measurements. *Radio Science*, *49*(11), 1124–1139. https://doi.org/10.1002/2014RS005519

Nishimura, Y. (2021). Basic concepts and overview of the coupling system. In Y. Nishimura, Y. Deng, O. Verkhoglyadova, & S. Zhang (Eds.), *Multi-scale Magnetosphere-Ionosphere-Thermosphere Coupling Chapter 1 Part I*. Elsevier. https://doi.org/10.1016/B978-0-12-821366-7.00007-X

Nishimura, Y. (2024). SuperDARN SECS velocity vectors [Dataset]. *Zenodo*. https://doi.org/10.5281/zenodo.11388708

Nishimura, Y., Deng, Y., Lyons, L. R., McGranaghan, R. M., & Zettergren, M. D. (2021). Multiscale dynamics in the high-latitude ionosphere. In C. Huang & G. Lu (Eds.), *AGU Space Physics and Aeronomy, Volume 3, Ionosphere Dynamics and Applications*, *Geophysical Monograph* (Vol. 260, pp. 49–65). American Geophysical Union Monograph. https://doi.org/10.1002/9781119815617.ch3

Nishimura, Y., Lyons, L., Zou, S., Angelopoulos, V., & Mende, S. (2010). Substorm triggering by new plasma intrusion: THEMIS all-sky imager observations. *Journal of Geophysical Research*, *115*(A7), A07222. https://doi.org/10.1029/2009ja015166

Nishimura, Y., Lyons, L. R., Angelopoulos, V., Kikuchi, T., Zou, S., & Mende, S. B. (2011). Relations between multiple auroral streamers, pre-onset thin arc formation, and substorm auroral onset. *Journal of Geophysical Research*, *116*(A9), A09214. https://doi.org/10.1029/2011JA016768

Nishimura, Y., Lyons, L. R., Zou, S., Xing, X., Angelopoulos, V., Mende, S. B., et al. (2010). Preonset time sequence of auroral substorms: Coordinated observations by all-sky imagers, satellites, and radars. *Journal of Geophysical Research*, *115*(A5), A00I08. https://doi.org/10.1029/2010JA015832

Nishimura, Y., Lyons, L. R., Zou, Y., Oksavik, K., Moen, J. I., Clausen, L. B., et al. (2014). Day-night coupling by a localized flow channel visualized by polar cap patch propagation. *Geophysical Research Letters*, *41*(11), 3701–3709. https://doi.org/10.1002/2014gl060301

Nishimura, Y., Wygant, J., Ono, T., Iizima, M., Kumamoto, A., Brautigam, D., & Friedel, R. (2008). SAPS measurements around the magnetic equator by CRRES. *Geophysical Research Letters*, *35*(10), L10104. https://doi.org/10.1029/2008GL033970

Ozturk, D. S., Meng, X., Verkhoglyadova, O. P., Varney, R., Reimer, A. S., & Semeter, J. L. (2020). A new framework to incorporate high-latitude input for mesoscale electrodynamics. *Journal of Geophysical Research: Space Physics*, *125*(1), e2019JA027562. https://doi.org/10.1029/2019ja027562

Papitashvili, N. E., & King, J. H. (2020). Solar wind and geomagnetic indices [Dataset]. *NASA Space Physics Data Facility*. Retrieved from https://cdaweb.gsfc.nasa.gov/pub/data/omni/high_res_omni/

Pritchett, P. L., & Lu, S. (2018). Externally driven onset of localized magnetic reconnection and disruption in a magnetotail configuration. *Journal of Geophysical Research: Space Physics*, *123*(4), 2787–2800. https://doi.org/10.1002/2017ja025094

Richmond, A. D., & Kamide, Y. (1988). Mapping electrodynamic features of the high-latitude ionosphere from localized observations: Technique. *Journal of Geophysical Research*, *93*(A6), 5741–5759. https://doi.org/10.1029/JA093iA06p05741

Rideout, W. (1980). DMSP satellite HDF5 data [Dataset]. *Open Madrigal*. Retrieved from http://cedar.openmadrigal.org/list

Ruohoniemi, J. M., & Baker, K. B. (1998). Large-scale imaging of high-latitude convection with Super Dual Auroral Radar Network HF radar observations. *Journal of Geophysical Research*, *103*(A9), 20797–20811. https://doi.org/10.1029/98JA01288

Sheng, C., Deng, Y., Chen, Y.-J., Heelis, R. A., & Huang, Y. (2019). Effects of alignment between particle precipitation and ion convection patterns on Joule heating. *Journal of Geophysical Research: Space Physics*, *124*(6), 4905–4915. https://doi.org/10.1029/2018ja026446

Southwood, D. J., & Kivelson, M. G. (1993). Aspects in common of high latitude ionospheric vortex motions. *Advances in Space Research*, *13*(4), 149–157. https://doi.org/10.1016/0273-1177(93)90328-9

Strang, G. (2016). *Introduction to linear algebra*. Cambridge Press.

Thomas, E. G., & Shepherd, S. G. (2018). Statistical patterns of ionospheric convection derived from mid-latitude, high-latitude, and polar SuperDARN HF radar observations. *Journal of Geophysical Research: Space Physics*, *123*(4), 3196–3216. https://doi.org/10.1002/2018ja025280

Tsyganenko, N. A. (2002). A model of the near magnetosphere with a dawn-dusk asymmetry, 2, Parameterization and fitting to observations. *Journal of Geophysical Research*, *107*(A8), SMP 10-1–SMP 10-17. https://doi.org/10.1029/2001JA000220

Vanhamäki, H., & Juusola, L. (2020). Introduction to spherical elementary current systems. In M. Dunlop & H. Lühr (Eds.), *Ionospheric Multi-Spacecraft Analysis Tools*, *ISSI Scientific Report Series* (Vol. 17, pp. 5–33). Springer. https://doi.org/10.1007/978-3-030-26732-2_2

Weimer, D. R. (2005). Improved ionospheric electrodynamic models and application to calculating Joule heating rates. *Journal of Geophysical Research*, *110*(A5), A05306. https://doi.org/10.1029/2004JA010884

Wu, H., & Lu, X. (2022). Data assimilation of high-latitude electric fields: Extension of a multi-resolution Gaussian process model (Lattice Kriging) to vector fields. *Space Weather*, *20*(1), e2021SW002880. https://doi.org/10.1029/2021sw002880

Yang, J., Toffoletto, F. R., Wolf, R. A., & Sazykin, S. (2015). On the contribution of plasma sheet bubbles to the storm time ring current. *Journal of Geophysical Research: Space Physics*, *120*(9), 7416–7432. https://doi.org/10.1002/2015JA021398

Yeoman, T. K., Chisham, G., Baddeley, L. J., Dhillon, R. S., Karhunen, T. J. T., Robinson, T. R., et al. (2008). Mapping ionospheric backscatter measured by the SuperDARN HF radars – Part 2: Assessing SuperDARN virtual height models. *Annales Geophysicae*, *26*(4), 843–852. https://doi.org/10.5194/angeo-26-843-2008

Zou, S., Lyons, L. R., & Nishimura, Y. (2013). Mutual evolution of aurora and ionospheric electrodynamic features near the Harang reversal during substorms, *Auroral phenomenology and magnetospheric processes: Earth and other planets* (pp. 159–170). https://doi.org/10.1029/2011GM001163